processes

Article

Effect of Closure Characteristics of Annular Jet Mixed Zone on Inspiratory Performance and Bubble System

Chao Wang [1], Chuanzhen Wang [1,2,*], Anghong Yu [1], Mingdong Zheng [1] and Md. Shakhaoath Khan [3,*]

1 State Key Laboratory of Mining Response and Disaster Prevention and Control in Deep Coal Mines, College of Material Science and Engineering, Anhui University of Science and Technology, Huainan 232001, China; oppooppo5@163.com (C.W.); yuanghong1006@163.com (A.Y.); mdzheng@aust.edu.cn (M.Z.)

2 Key Laboratory of Coal Processing and Efficient Utilization, Ministry of Education, Xuzhou, China University of Mining and Technology, Xuzhou 221116, China

3 Department of Chemical Engineering, Monash University, Clayton, VIC 3800, Australia

* Correspondence: faxofking@cumt.edu.cn (C.W.); ms.khan@monash.edu (M.S.K.); Tel.: +86-18852146286 (C.W.); +61-(3)-9905-6003 (M.S.K.)

Abstract: In the flotation process, gas-liquid properties and the bubble system greatly influence bubble mineralization. In order to clarify how the mechanism applies to the closure characteristics of an annular jet mixed flow zone on the inspiratory performance and the bubble system, different degrees of closure on the velocity field and gas-liquid ratio in the mixed flow zone were investigated using numerical simulation. The variations in the characteristics of bubble size distribution, rising velocity, and gas content under different closure levels were measured with a high-speed dynamic camera technology. The results confirmed that when the closure degrees of the mixed flow zone improved, the inlet jet could gradually overcome the static pressure outside the nozzle effectively. It formed a gas-liquid mixing zone with high turbulence first, and a large pressure difference at the gas-liquid junction second. This helped to increase the inspiratory capacity. At the same time, the gas-liquid ratio rose gradually under conditions of constant flow. When the nozzle outlet was completely closed, the gas-liquid ratio gradually stabilized. For the bubble distribution system, an enhancement in the closure degrees can effectively reduce the bubble size, and subsequently, the bubble size distribution became more uniform. Due to the improved gas-liquid shear mixing, the aspect ratio of the bubbles can be effectively changed, consequently reducing the bubble rising speed and increasing the gas content and bubble surface area flux of the liquid.

Keywords: numerical simulation; closure characteristics; bubble size distribution; gas content; bubble surface area flux

check for updates

Citation: Wang, C.; Wang, C.; Yu, A.; Zheng, M.; Khan, M.S. Effect of Closure Characteristics of Annular Jet Mixed Zone on Inspiratory Performance and Bubble System. *Processes* **2021**, *9*, 1392. https://doi.org/10.3390/pr9081392

Academic Editor: George Z. Kyzas

Received: 28 June 2021
Accepted: 9 August 2021
Published: 11 August 2021

1. Introduction

Flotation is an effective way to treat fine coal slime [1–3]. The suction performance of flotation equipment and the characteristics of the bubble system significantly impact the flotation effect [4–6]. Currently, the most commonly used slime flotation equipment includes the mechanical flotation machine and flotation column. There are two types of mechanical flotation machine: one is a mechanical stirring air suction flotation machine, and the other is a jet air suction flotation machine. The biggest difference between these types of flotation machines is that the suction mode varies. When the mechanical stirring air suction flotation machine is operating, the impeller stirs the pulp and throws the pulp around the impeller. The area under the impeller is characterized by low pressure and inhales air, which will produce a large number of bubbles [7]. When the jet air suction flotation machine is functioning, the velocity difference between the high-pressure pulp flow and the air flow makes it possible for the air to enter the jet core area under pressure. The flotation column contains no moving parts and the bubbles rely on external input. The flotation process relies on the rising of a group of bubbles (with hydrophobic particles) and the settlement of hydrophilic particles [8].

The suction capacity of the mechanical stirring air suction flotation machine remains stable, but the suction effect is greatly affected by the structure of the impeller stator system [9]. Due to the mechanical stirring of the impeller stator, the energy consumption of this flotation machine is also greater [10]. The jet air suction flotation machine has a large suction capacity and does not consume much energy, but its suction mode determines that there will be a large number of small bubbles in the suction process, and the suction effect is unstable [11]. The air intake of the flotation column depends on external equipment, and the stability of the bubble particle contact process is closely linked to the height of the flotation column [8].

Regardless of whether jet flotation or stirring flotation is being used, bubbles will be produced in what is known as the carrier of the flotation process [12]. Results show that the formation of the bubble system is affected by many factors. The foaming agent affects the bubble mineralization process and bubble movement characteristics [13,14]. The bubble size is greatly shaped by the concentration of the foaming agent. Within a certain range, an increase in the foaming agent concentration leads to a diminished bubble size. When the foaming agent reaches a certain concentration, the bubble size tends to remain stable [15,16], and the bubble size will affect its rising speed [17–19]. The pressure field also has an important influence on the formation of the bubble system and exists in many forms. Impeller stirring is a kind of pressure field that can change the shape of the bubble system. It can destroy the gas-liquid interface by changing the turbulent state of fluid, significantly change the size of bubbles, and affect the whole flotation process.

As an application of the induced jet, not only can the annular submerged jet be used for suction, but it can also exert a significant impact on the formation of the bubble system, thus affecting the flotation efficiency. At present, the annular jet is used in the jet flotation machine, flotation column, and other equipment. Research conducted by domestic and foreign scholars has mainly focused on the analysis of the gas-liquid two-phase flow field and the optimization of structural parameters. Research has shown that the high-speed jet of the main nozzle of the suction nozzle causes gas flow compression, and then a change in the liquid phase. The phase change performance and gas-liquid mixing performance of the nozzle can be effectively altered by transforming the area ratio [20]. In addition, the diameter of the droplet size and the existence of microbubbles greatly influence the characteristics of the jet flow [21]. Some experts have conducted extensive simulations and experiments on the outlet structure, mixing zone structure, and positioning design of the bypass suction pipe of the R77 ejector, in an effort to realize better nozzle suction performance and efficiency [22,23]. Similarly, other researchers have studied the evolution process in the gas-liquid submerged jet. Their work has shown that the pipe inner diameter, suspension height, and initial gas surface velocity are three important parameters affecting the nozzle suction [24].

A new method of annular jet control based on secondary fluid cross-injection was proposed in [25]. The nozzle designed by the author has a specific geometry and functions by connecting the annular jet and the nozzle cone when cross-flow injection is applied. This study highlighted in detail the physical process of the transition from the additional jet to the wall jet. The annular nozzle used in one paper [26] was designed with an active flow control system, which uses 12 synthetic jets to eject radially from the central nozzle body. It also measures the control effect on the impact wall, focusing on the generation and control of the annular impinging jet.

Combined with the existing research that has been published on this subject, this paper used the numerical simulation method to explore the influences of different sealing degrees on the pressure field and gas-liquid ratio in the mixed flow area of the annular jet nozzle. At the same time, combined with the high-speed dynamic camera, the variation characteristics of bubble size distribution, rising speed, and bubble surface area flux under different sealing degrees were measured. The overarching objective was to enable efficient mineralization flotation.

2. Test Device and Numerical Model

2.1. Test Device

Figure 1a shows the test system, one that is mainly composed of a submerged jet device and bubble measuring device, which can measure the suction volume, and also collect and measure bubbles. The system mainly includes the following components: (1) an observation tank, (2) an overflow tank, (3) an overflow pipe, (4) a circulation tank, (5) a circulation pump, (6) an electromagnetic flowmeter, (7) a pressure gauge, (8) an annular jet nozzle, (9) an air flow meter, (10) a high-speed dynamic camera, and (11) a light source. The annular jet nozzle, as shown in Figure 1b, has many components, for instance: (12) a feed tube, (13) nozzle exit, (14) mixed flow zone a, (15) mixed flow zone b, (16) an aspirating pipe, (17) a metallic gasket, and (18) a connection pipe. The feed pipe outlet diameter m is 8 mm while the inlet diameter n is 12 mm. The light source used in the experiment is a quartz lamp produced by OSRAM, Germany. The model of the light source is BL-1000 A and the energy is 1000 W.

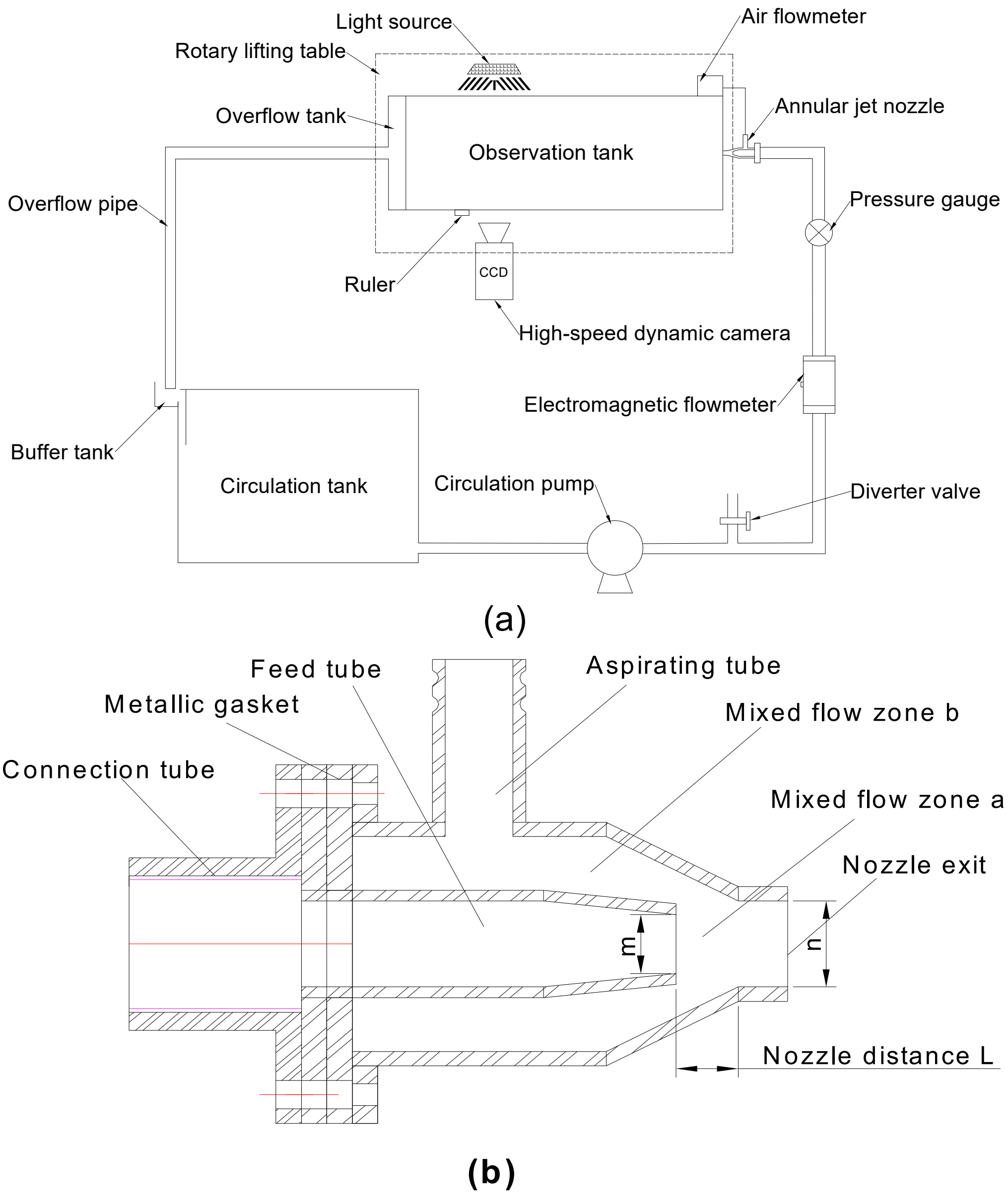

Figure 1. Experimental test system. (**a**) Diagram of test system; (**b**) structural diagram of annular jet nozzle.

The inlet pressure P of the feed pipe can be adjusted by the diverter valve so that it stays at 0.10 MPa. The nozzle distance L can be adjusted by the metallic gasket and the adjustment range is 0–20 mm. The observation tank is made of highly transparent glass, which is used for submerged jet and bubble collection. The length, width, and height of the glass tank are 70 cm, 15 cm, and 40 cm, respectively.

As shown in Figure 1a, the overflow tank is located at the overflow outlet end of the observation tank, with a length of 50 mm, width of 150 mm, and height of 200 mm, respectively, and the outlet hole diameter of the overflow tank is 32 mm. Restricted by the nozzle manufacturing process, but also to ensure the full diffusion of the submerged jet, the size of the observation tank used in this measurement is larger. In the measurement, in order to ensure that the bubble measurement does not lose focus, the matching between the brightness of the backlight and focal length is debugged, so that the outline of the bubble can be photographed well. The captured and processed sample images of bubbles are shown in Figure 2. The bubble size calibration method involves placing a steel ruler with a width of 35 mm on the inner surface of the steel tank as the standard for calibrating the bubble size.

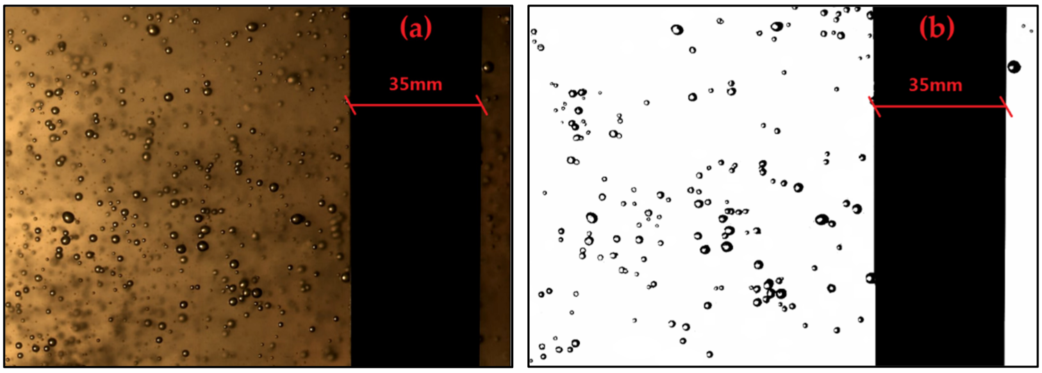

Figure 2. Captured and processed sample images of bubbles. (**a**) Original image of bubbles. (**b**) Processed image of bubbles' contours.

2.2. Test Process

While the system is operating, the observation tank (1) and circulation tank (4) are filled with a foaming agent solution, the circulation pump (5) will feed water to the annular jet nozzle (8), and the negative pressure of the jet will suck air into the feed pipe (12) from the aspirating pipe (15), and mix with the solution. In this way, a large number of bubbles will be generated in the mixing flow zone of the nozzle exit (13). After the system becomes stable for about one minute, the backlight is shone on the observation surface on one side of the observation tank (1). As the light source (11) placed on one side is pasted with light cloth oil paper, the brightness distribution is uniform. On the other hand, a high-speed dynamic camera (10) is set-up and directly opposite to the light source (11). The camera focuses on capturing the clear bubble shape and change process. At the same time, the air flow rate and the outlet flow rate of the annular jet nozzle (8) are obtained by an air flowmeter and electromagnetic flowmeter, respectively.

During the test, the submergence depth of the annular jet nozzle (8) is 150 mm, while the pressure of the pressure gauge (7) remains unchanged. The closure degree of the inlet jet to the nozzle exit outlet is adjusted by adjusting the distance between the feed pipe (12) and the nozzle exit (13) outlet. The opening of the liquid level-regulating valve serves to control the liquid level in the observation tank (1), in order for it to be filled with clear water medium.

Because it is difficult to measure the bubble production process in the gas-liquid mixing state in the annular jet nozzle (8), the bubbles produced are released into the tank and then measured. Due to the effect of the bubble group dissolving and merging in the tank, this will affect the measurement and characterization of the bubble system generated by the annular jet nozzle (8). In order to better understand the influence of the annulus jet on the characteristics of the bubble system in the observation tank (1), the effect of the bubble merger was minimized by using a foaming agent concentration greater than the critical coalescence concentration. The experimental solution with a concentration greater than the critical coalescence concentration was prepared by deionized water serving as the medium. Subsequently, the concentration was 0.13 mmol/L and the average temperature required for the test was 25 °C.

When shooting bubbles, the image acquisition frequency was 1000 frames/s, and ProAnalyst software (2-D Professional, Woburn, MA, USA) was used for processing. At least 2000 bubbles were analyzed in each group.

Considering that the same bubbles may be captured in continuous images, the shooting time in each case lasted 2 min or more, and an area of 80 mm by 80 mm was effectively focused on and photographed. As the rising velocity of bubbles was distributed between 260 and 290 cm/s, the interval between the two selected pictures in shooting time should be at least 0.04 s when selecting the pictures for bubbles recognition and statistics, to ensure that the same bubble is not measured repeatedly. At the same time, 50 pictures in each case were selected to ensure that the number of bubbles reached 2000. Figure 2 depicts the captured and processed sample image of bubbles. Figure 2a shows the original image while Figure 2b shows the bubbles' contour image processed by the software.

The Sauter diameter helped to characterize the bubble size characteristics in the test, which can be calculated by the following formula [27]:

$$D_{32} = \frac{\sum_{i=1}^{n} n_i d_{bi}^3}{\sum_{i=1} n_i d_{bi}^2} \quad (1)$$

where d_{bi} is the bubble diameter and n_i is the number of bubbles.

The suction characteristics of the annular jet nozzle can be evaluated by the relationship curve q between the gas-liquid ratio and suction volume:

$$q = \frac{Q_g}{Q_l} \quad (2)$$

where Q_g and Q_l are the volume flows of gas and water, respectively. The suction capacity Q_g can be obtained by a gas flow meter (9), and the volume flow quantity Q_l can be obtained by an electromagnetic flow meter. The model type of the gas flow meter (9) was LZB-4, which is manufactured by China Hongqi Instrument Co., Ltd. (Wenzhou, China) and the measuring range is 25–250 L/h.

2.3. Reagents

The foaming agent used in this study was MIBC, which is produced by Shanghai Hans Chemical Co., Ltd. (Shanghai, China). The molecular formula is (CH3)2CHCH2CH(OH)CH3 and the molecular weight is 102.18. The density, viscosity, and surface tension of the foaming agent were, respectively, 0.8033, 4.59 mPa·s, and 25.3 dyne/cm.

3. Numerical Model

Model Establishment

The three-dimensional model for the annular jet nozzle and observation slot was established. In order to improve the model's mesh quality, a structured mesh was used in the ejector pipe, nozzle, mixing zone, and slot, while an unstructured tetrahedral mesh was employed in other parts of the annular jet device, such as the intersection of the slot and nozzle. The number of meshes used in the three-dimensional method was 980784.

Figure 3 shows the meshing diagram of the nozzle and observation tank. Figure 3a shows the combined meshing diagram of the observation tank and annular jet nozzle, while Figure 3b shows the meshing diagram of the annular jet nozzle.

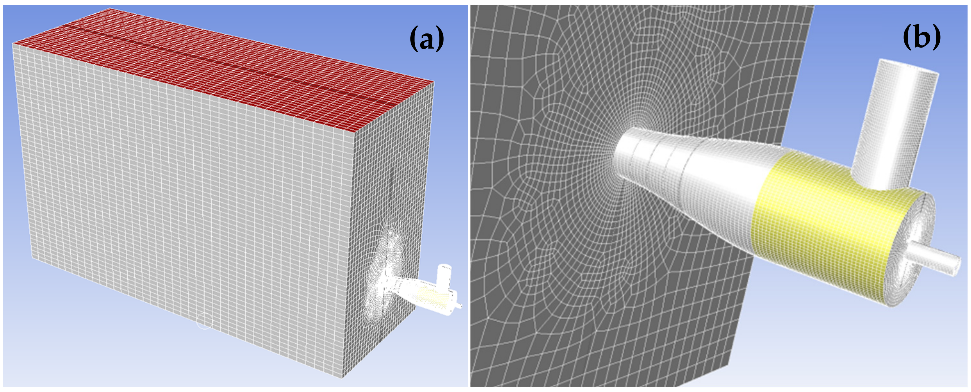

Figure 3. Meshing diagram of nozzle and observation tank. (**a**) Combined meshing diagram of observation tank and annular jet nozzle. (**b**) Meshing diagram of annular jet nozzle.

The boundary conditions were as follows: the turbulent intensity was 5%, and the turbulent viscosity ratio was 10. The turbulent viscosity ratio refers to the ratio of turbulent viscosity to dynamic viscosity. The inlet of the feed tube and the aspirating tube was a pressure inlet, and the outlet of the nozzle was also a pressure outlet. The inlet pressure of the feed tube was 0.10 MPa, the inlet pressure of the aspirating tube was 0 MPa, and outlet pressure of the nozzle was 0 MPa. The wall of the nozzle was a stationary wall and no slip shear condition. The numerical calculation of the annular jet device used a realizable turbulence model; the pressure velocity coupling term used the SIMPLEC algorithm [28,29]. For the multi-phase flow model, the VOF model can be used for the system where air and water cannot be integrated with each other. In this paper, the VOF model simulated the gas-liquid two-phase flow [30–32]. The coordinate origin of the geometric model was located in the center of the intersection of the nozzle and the ejector tube, with the exit direction of the ejector tube as the positive x direction. Meanwhile, the Z-axis was parallel to the suction tube and perpendicular to the X-axis.

4. Analysis of Results

4.1. Evaluating the Reliability of Numerical Simulation

The suction capacity and gas-liquid ratio of the annular jet nozzle with different tube-nozzle distances were measured by the test system when the inlet pressure was 0.10 MPa, and they were compared with the simulation test results. The outcomes are shown in Table 1.

Table 1. Numerical calculation design and the results.

	0.10 MPa (EXP)					**0.10 MPa (CFD)**				
	0	**3**	**7**	**15**	**20**	**0**	**3**	**7**	**15**	**20**
Q_g (m^3/h)	0.063	0.094	0.118	0.171	0.173	0.060	0.090	0.110	0.162	0.170
Q_l (m^3/h)	0.422	0.541	0.543	0.557	0.559	0.421	0.542	0.544	0.553	0.561
q	0.149	0.174	0.217	0.307	0.309	0.143	0.166	0.202	0.293	0.303

The equation between nozzle distance L and suction capacity is obtained via cubic polynomial regression analysis:

$$Q_{gCFD} = -8 \times 10^{-6} \times L^3 + 6 \times 10^{-5} \times L^2 + 0.0074 \times L + 0.062 \left(R^2 = 0.9938\right)$$

$$Q_{gEXP} = -1 \times 10^{-5} \times L^3 + 0.0001 \times L^2 + 0.0079 \times L + 0.0648 \left(R^2 = 0.9953\right)$$

The cubic polynomial regression equation between nozzle distance L and gas-liquid ratio q is as follows:

$$q_{CFD} = -4 \times 10^{-5} \times L^3 + 0.001 \times L^2 + 0.0036 \times L + \ 0.1438 \left(R^2 = 0.9989\right)$$

$$q_{EXP} = -4 \times 10^{-5} \times L^3 + 0.001 \times L^2 + 0.0047 \times L + \ 0.1499 \left(R^2 = 0.9998\right)$$

The subscript sum represents the numerical analysis value and the experimental value, respectively. The prediction error of numerical calculation and experiment is obtained by using a dimensionless equation:

$$\alpha_{Q_g} = \frac{Q_{gCFD} - Q_{gEXP}}{Q_{gEXP}} \times 100\%$$

$$\alpha_q = \frac{q_{CFD} - q_{EXP}}{q_{EXP}} \times 100\%$$

The nozzle distance ranged from 0 to 20 mm, the corresponding α_{Qg} value was about 5.2%, and the α_q value was about 4.8%. Consequently, it can be stated that the numerical model had high reliability.

Figure 4 illustrates the comparison between the numerical simulation and experimental test. It is observed that with the increase in nozzle distance, the suction capacity and gas-liquid ratio increased as the inlet pressure also increased. The suction capacity rose from 0.063 m^3/h when the nozzle distance was 0 mm to 0.173 m^3/h when the nozzle distance was 20 mm, with an increase of 174.60%. The gas-liquid ratio also rose from 0.149 to 0.309, with an increase of 107.38%. This confirms that the nozzle distance and inlet pressure had an important influence on the adjustment of suction volume and gas-liquid ratio.

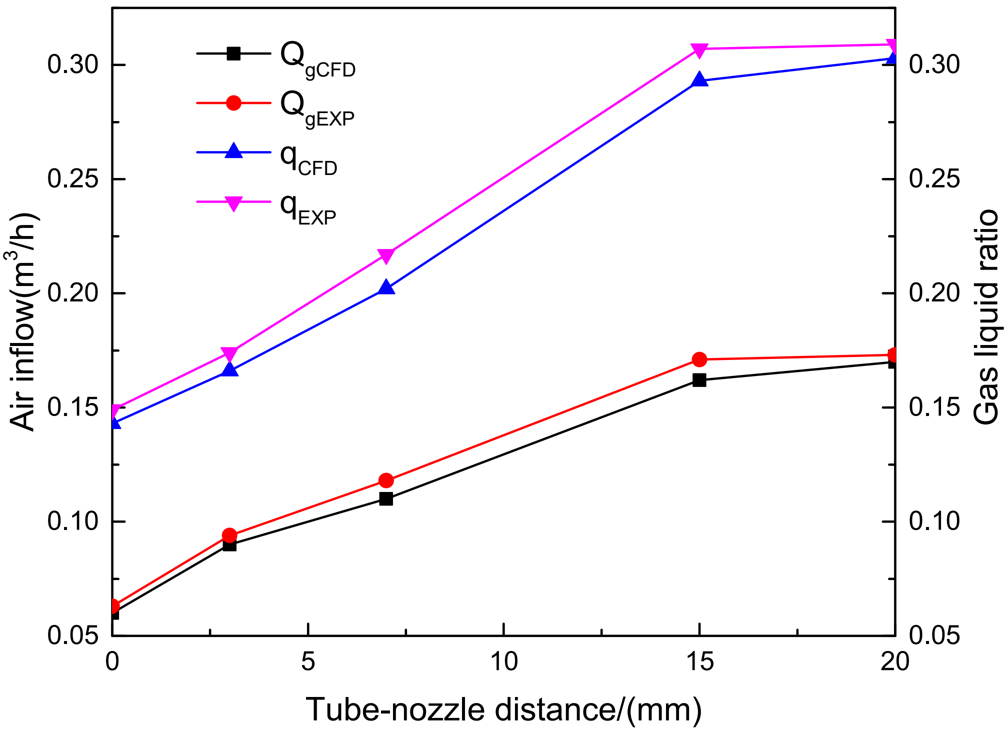

Figure 4. Comparison of numerical model and experiment.

At the same time, it can be seen that due to the closure of the nozzle outlet by the diffusion water beam, an effective mixed flow zone formed, which improved the suction capacity. Therefore, the gas-liquid ratio can be effectively adjusted by controlling the suction capacity from the outside, and then the gas holdup of the slurry can be controlled. At the same time, as the nozzle distance continued to increase, the gas-liquid ratio and suction rate diminished. This is due to the fall in velocity difference on the one hand, and the backmixing of the feed on the inner wall of the nozzle on the other.

4.2. Analysis of Internal Flow Field

4.2.1. Variation Characteristics of Velocity Field under Different Tube-Nozzle Distances

Figure 5 shows the velocity vector diagram of the gas–water mixed phase in the nozzle with different nozzle distances. In different areas of the nozzle, the proportion of the gas phase or liquid phase was different. It can be seen from Figure 5a that when the tube-nozzle distance expanded from 0 mm to 20 mm, the core flow velocity increased from 10.75 m/s to 14.28 m/s, the maximum flow velocity in the mixed flow zone also increases from 1.07 m/s to 3.57 m/s, and the suction capacity increased from 0.063 m^3/h to 0.173 m^3/h. Based on what is shown in the velocity vector diagram, it appears that when there was a larger nozzle distance, the range of the mixed flow zone increased. At this time, the maximum water velocity in the core of the feed flow did not change, but the water velocity in the radial direction gradually reduced with the increase in axial distance.

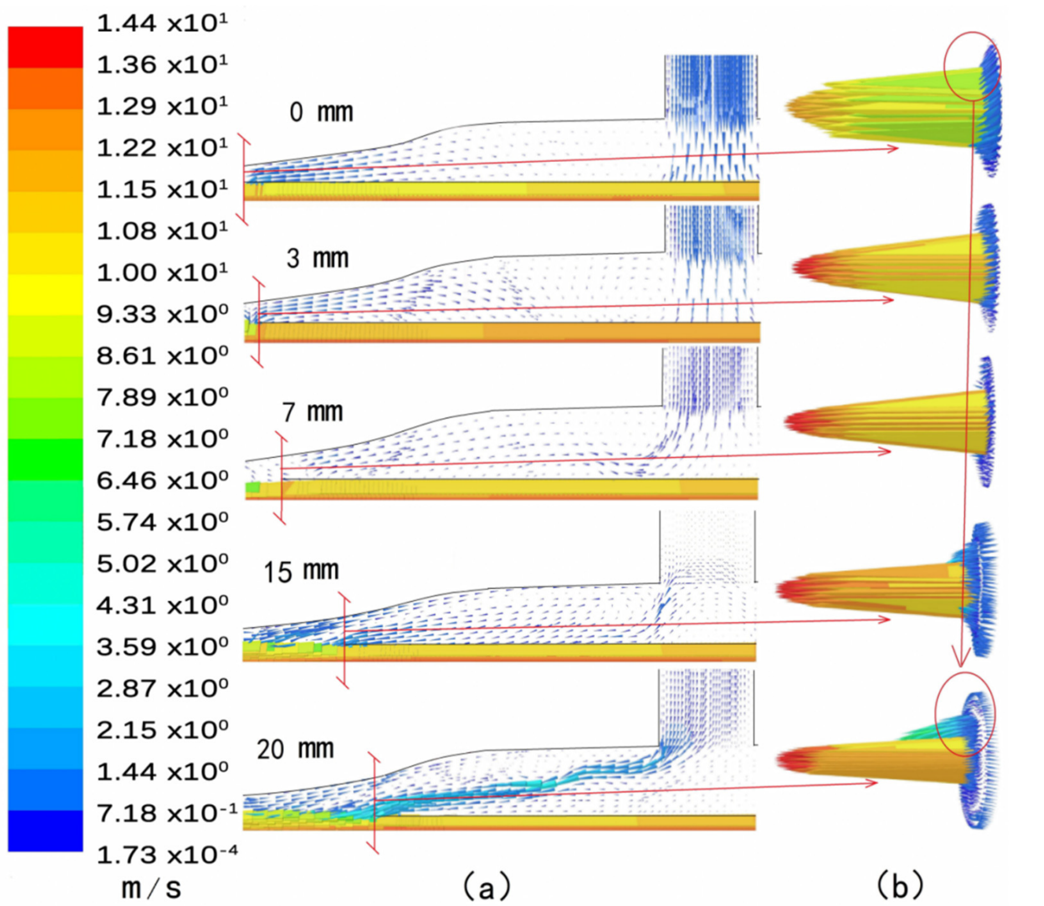

Figure 5. Velocity vector diagram of gas–water mixed phase in nozzle with different nozzle distances. (**a**) Velocity vector diagram of Y = 0. (**b**) Velocity vector diagram of the junction of mixed flow area a and mixed flow area b.

There is a certain diffusivity of the water beam in the process of the submerged jet. According to the schematic diagram of the water beam sealing process at the nozzle outlet (Figure 6), when the nozzle distance was short, the diffusivity of the water beam close to the outlet was low, and the water beam failed to prevent the water in the water tank from entering the nozzle. The mixed flow area a was very small, so it was impossible to form an effective pressure difference at the junction of mixed flow area a and mixed flow area b, as shown in Figure 6a. With the increase in nozzle distance, the increase in water beam cross-sectional area can effectively seal the nozzle outlet. This helps to overcome the static pressure of water in the tank and form a large velocity difference at the junction of mixed flow area a and mixed flow area b, effectively forming a large pressure difference. At the same time, the more obvious the ejection effect is in the mixed flow zone b, the more air suction can be obtained by forming an air flow belt, as shown in Figure 6b. This is consistent with the direction of the jet. It can also be seen from the vector diagram of the junction of mixed flow area a and mixed flow area b shown in Figure 5b that the gas region and velocity vector in the radial direction gradually increased.

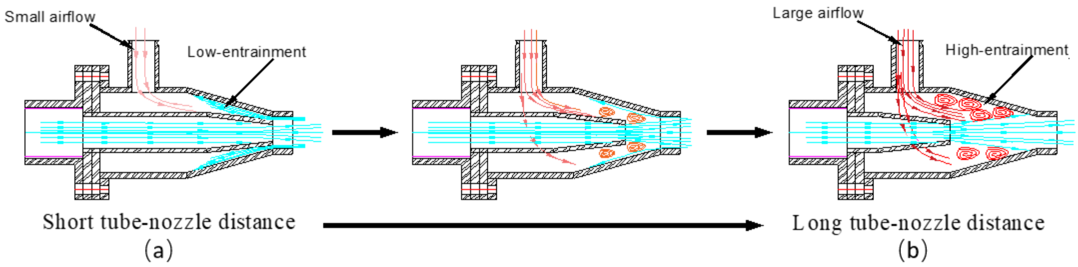

Figure 6. Effect of nozzle outlet closure degree on suction and vorticity variation under different tube-nozzle distances. (**a**) Diagram of suction and vorticity variation under short tube-nozzle distances. (**b**) Diagram of suction and vorticity variation under long tube-nozzle distances.

Based on the gas-liquid two-phase volume division diagram at different tube-nozzle distances shown in Figure 7, it can be observed that as the tube-nozzle distance increased, the nozzle mixing zone a and mixing zone b within the volume of the liquid phase gradually diminished. The gas phase volume accounted for more and more, and the airflow band gradually formed in mixing zone b, and while the suction volume and gas-liquid ratio increased, the gas interacted directly with the feed stream in mixing zone a. This produced small bubble clusters after shearing and breaking, and then initially forming a bubble system, which helps bubbles disperse better in the tank carried by the jet.

4.2.2. Influence of Inflow Pressure on Bubble Size Distribution

Figure 8 depicts the change curve of bubble particle size distribution under different tube-nozzle distances, and Figure 8a highlights the bubble probability density distribution at 0.10 MPa. As the tube-nozzle distance increased, the distribution range of bubble size gradually decreased, the probability of smaller bubble particle size also increased, and the average bubble size decreased. For example, when the nozzle distance was 0 mm, the range of the bubble particle size distribution with a probability greater than 60% was 0.75~1.59 mm, and the particle size fluctuation range was 0.84 mm. When the nozzle distance increased to 20 mm, the bubble particle size distribution range was 0.47~1.22 mm with a probability greater than 60%, and the particle size fluctuation range was 0.75 mm. It is known that as the nozzle distance increased, the particle size shrank and became more uniform.

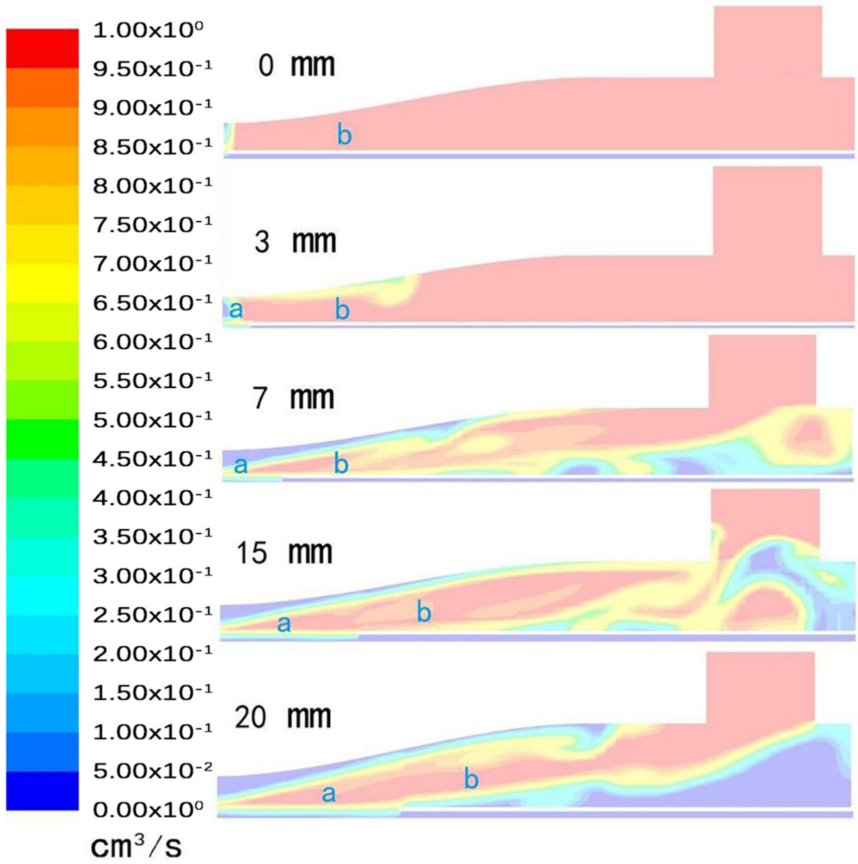

Figure 7. Distribution of volume fraction of gas-liquid under different tube-nozzle distances. Mixed flow zone a; mixed flow zone b.

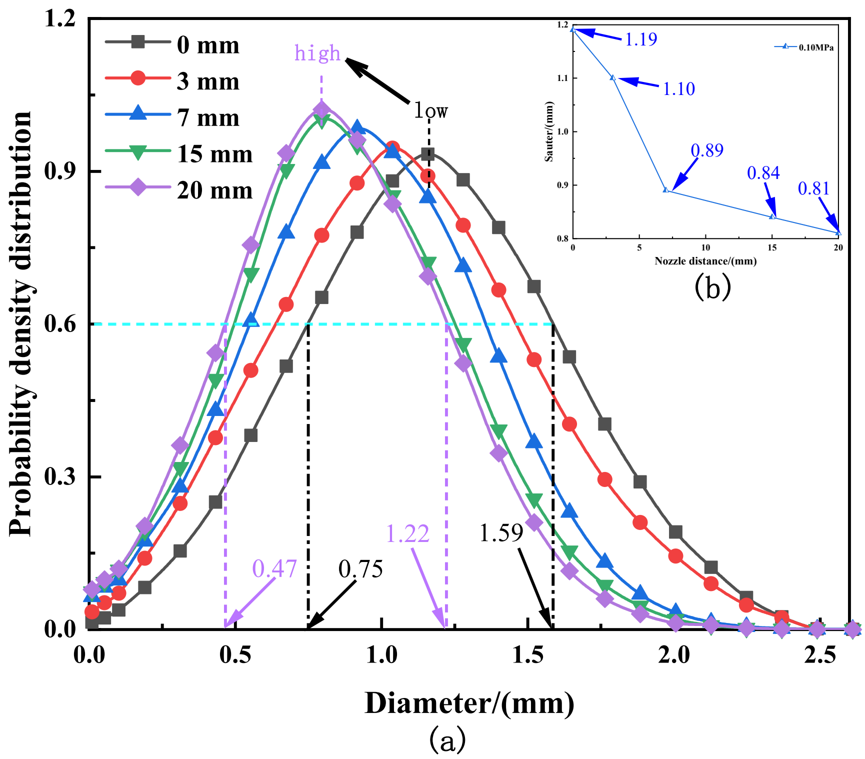

Figure 8. Influence of tube-nozzle distances on bubble size distribution. (**a**) Bubble probability density distribution at 0.10 MPa; (**b**) Sauter diameter variation of bubbles.

Figure 8b shows the variation curve of the bubble Sauter diameter, in which it can be seen that when the tube-nozzle distance increased, the Sauter diameter of the bubble decreased, while the particle size changed more when it switched from 0 to 7 mm. When the tube-nozzle distance reached 15 mm, the particle size of a bubble tended to be stable. Under the large nozzle distance, when the vortex formed at the mixing zone was large, the higher the degree of turbulence, the stronger the shearing effect, and the smaller the diameter of the bubbles formed.

5. Effect of Tube-Nozzle Distances on Bubble Motion Characteristics

The aspect ratio of the bubbles and the rising speed of the bubbles in water are directly related to the gas content and adsorption effect with the agent [19]. This study also discovered that the bubble rise velocity declined linearly with the increase in the aspect ratio, independent of the reagent type, concentration, and mixing. It is therefore necessary to study the influence of the nozzle outlet closure degree on the aspect ratio and bubble rise velocity at different tube-nozzle distances, in order to regulate the bubble system.

Figure 9 shows the influence curve of different tube-nozzle distances on the bubble aspect ratio and rising speed. As the tube-nozzle distance gradually increased, the gas-liquid mixing zone also gradually increased, and the incidence of the jet to the nozzle outlet closure enhanced, so the cutting and crushing effect on the bubble was reinforced. The bubble particle size reduced while the resistance to deformation strengthened, so the aspect ratio gradually increased, first from 0.74 of 0 mm to 0.93 of 20 mm. Eventually, they converged to the spherical variation range, while the bubble rising speed decreased with the tube-nozzle distance. Furthermore, the gas velocity decreased progressively and moderately when the tube-nozzle distance was greater than 7 mm. A lower bubble rising speed helps to improve the gas content of the pulp, which is then conducive to regulating the bubble mineralization time.

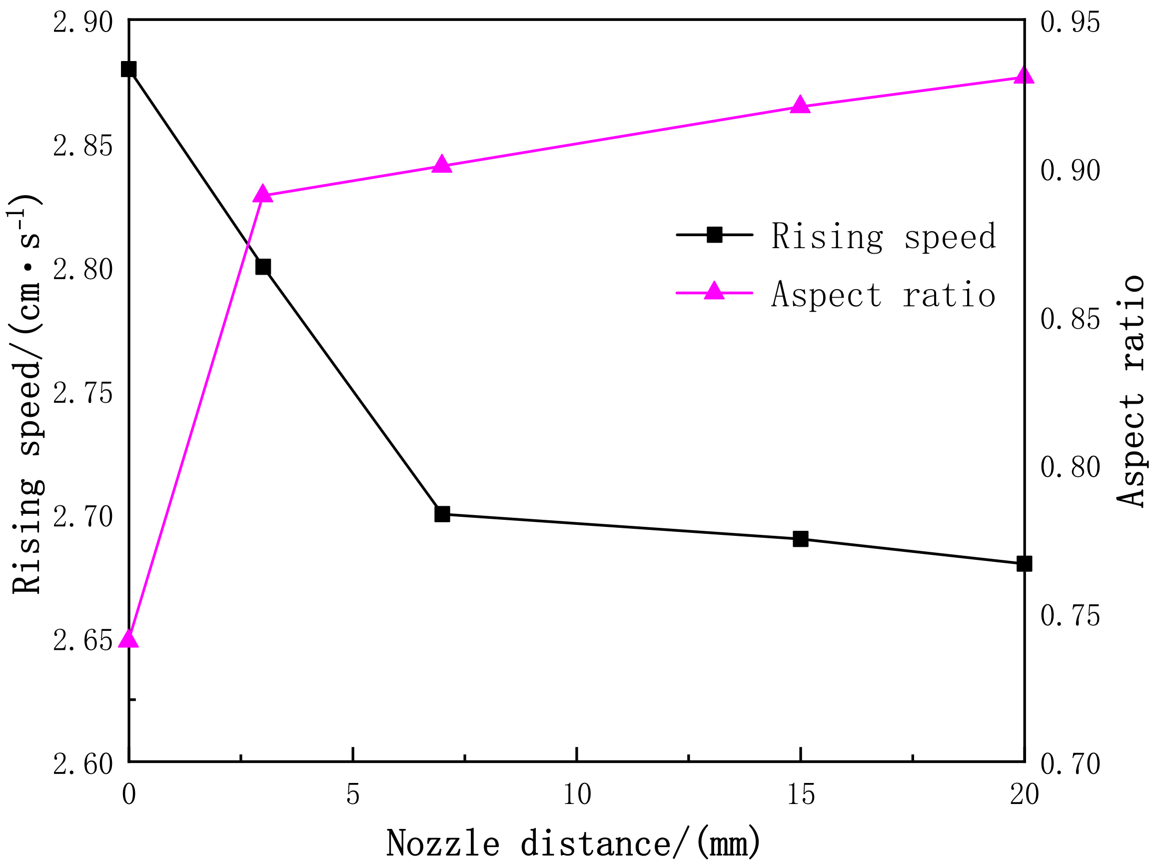

Figure 9. Effect of tube-nozzle distance on bubble aspect ratio and rise velocity.

6. Analysis of the Effect of Bubble Surface Area Flux

The surface area flux of bubbles expresses the surface area of bubbles passing through a unit cross-sectional area of the tank per unit time. It is important for the measurement of the bubble gas capacity and the adsorption surface of the agent. For the effect of bubble surface area, fluxes S_b were used [33]:

$$S_b = 6\frac{J_g}{D_{32}} \tag{3}$$

where J_g denotes the surface gas velocity and D_{32} denotes the Sauter diameter. The surface area flux of bubbles expresses the surface area of bubbles passing through a unit cross-sectional area of the tank per unit time. The surface flux can be used to characterize the number and diameter of bubbles. The increase in surface area flux means that there are more small-diameter bubbles in the liquid phase at a certain superficial gas velocity.

The comparative plots of bubble surface fluxes are derived from Equation (3) for the tube-nozzle distances of 0 mm and 20 mm, respectively, as shown in Figure 10.

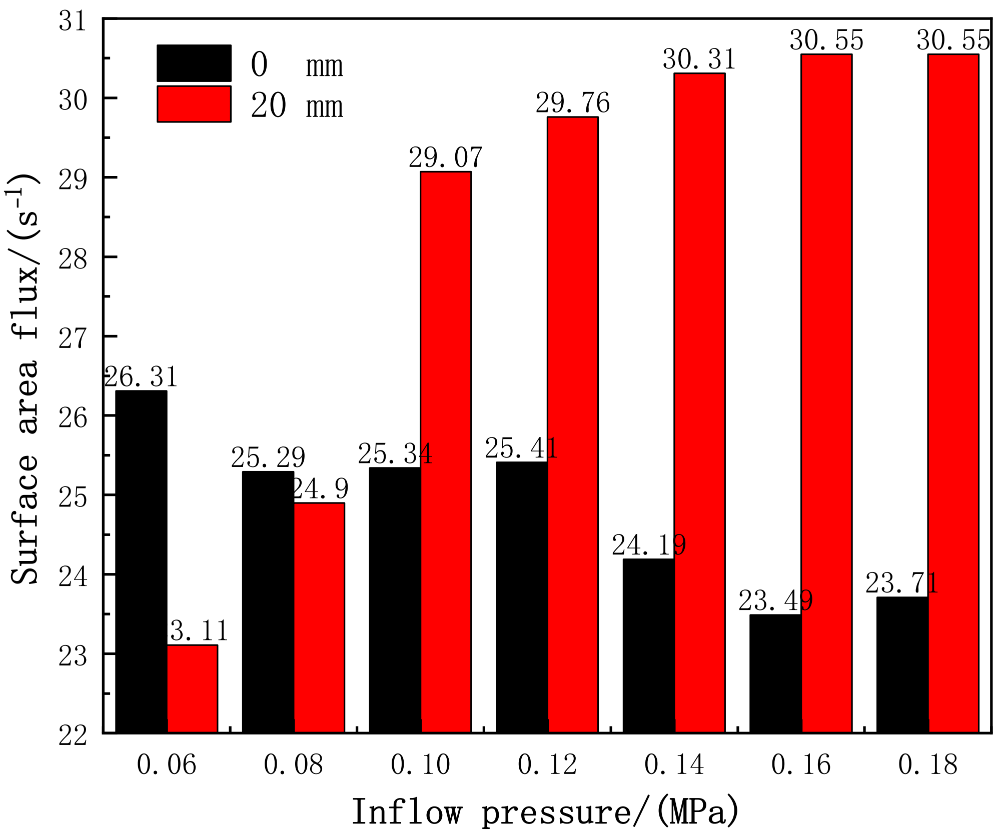

Figure 10. Influence of nozzle distance on bubble surface area flux.

The bubble surface area flux decreased and then stabilized to 23.11 s^{-1} with increasing tube-nozzle distance at smaller inflow pressures, while it increased and then stabilized to more than 30.00 s^{-1} with increasing tube-nozzle distance at larger inflow pressures. As indicated in Figure 8, when the tube-nozzle distance was 0 mm, the gas flux decreased, and the bubble surface area flux was low as the inflow pressure increased, remaining at about 23.00 s^{-1}. When the tube-nozzle distance was 20 mm, the bubble surface area flux increased as the inlet pressure rose and stabilized at about 30.55 s^{-1}; this occurred when the nozzle distance reached 7 mm. Based on the above analysis, it can be stated here that a smaller tube-nozzle distance was not conducive to improving the bubble surface area flux, while a higher tube-nozzle distance was certainly conducive to improving the bubble surface area flux. This is linked to the surface energy required for bubble rupture, and also indicates that the best parameter conditions will improve the surface area flux with the least energy consumption and provide the best results.

7. Conclusions

The results showed that with the change in nozzle distance, the closure degree of the nozzle outlet will also change, which will have a significant regulating effect on the inspiratory characteristics and motion characteristics.

1. From the velocity vector diagram of the flow field in the nozzle and the gas-liquid two-phase volume distribution diagram, the following could be seen: the feed stream in the submerged jet state; the core water velocity along the radial direction gradually spread; the closure of the nozzle outlet degree improved; the pressure difference at the junction of mixing zone a and mixing zone b also gradually increased. Furthermore, the suction performance, suction volume, and gas-liquid ratio were boosted.
2. The influence on the characteristics of the bubble system was also reflected in the degree of confinement of the inlet flow to the mixing zone. The greater the degree of confinement, the stronger the effect of entrainment and shear action in the mixing zone. Subsequently, the bubble size shrank and the particle size distribution was also more uniform.
3. Changing different tube-nozzle distances can effectively alter the suction performance and shear strength of the mixed flow area, and then the movement characteristics of the bubble can be adjusted. With a longer tube-nozzle distance, the nozzle outlet closure was enhanced, the bubble aspect ratio gradually increased, and the bubble rise speed gradually decreased. These aspects were conducive to improving the air content of the slurry. By studying the effect of different tube-nozzle distances on the bubble surface area flux, it can be concluded that a higher degree of closure helped to increase the bubble surface area flux.

Author Contributions: Conceptualization, C.W. (Chao Wang); data curation, C.W. (Chao Wang) and C.W. (Chuanzhen Wang); formal analysis, C.W. (Chuanzhen Wang) and A.Y.; funding acquisition, C.W. (Chao Wang); investigation, C.W. (Chao Wang) and C.W. (Chuanzhen Wang); methodology, C.W. (Chao Wang) and M.Z.; project administration, C.W. (Chuanzhen Wang) and M.S.K.; Software, C.W. (Chao Wang) and C.W. (Chuanzhen Wang); supervision, C.W. (Chuanzhen Wang) and M.S.K.; writing—original draft, C.W. (Chao Wang) and A.Y.; writing—review & editing, C.W. (Chao Wang) and C.W. (Chuanzhen Wang). All authors have read and agreed to the published version of the manuscript.

Funding: This work was financially supported by the research fund of the Provincial University Natural Science Research of Anhui (Grant No. KJ2018A0093), the Provincial Natural Science Foundation of Anhui Province of Anhui (Grant No. 1908085QE189), and the Postdoctoral Research Project of Anhui (Grant No. 2019B356).

Institutional Review Board Statement: Not applicable.

Informed Consent Statement: Not applicable.

Data Availability Statement: The data presented in this study are available on request from the corresponding author. The data are not publicly available due to the continuous research.

Conflicts of Interest: The authors declare no conflict of interest.

References

1. Zhu, H.; Valdivieso, A.L.; Zhu, J.; Song, S.; Min, F.; Arroyo, M.A.C. A study of bubble size evolution in Jameson flotation cell. *Chem. Eng. Res. Des.* **2018**, *137*, 461–466. [CrossRef]
2. Miettinen, T.; Ralston, J.; Fornasiero, D. The limits of fine particle flotation. *Miner. Eng.* **2010**, *23*, 420–437. [CrossRef]
3. Sahoo, S.K.; Suresh, N. Recovery of coal values from the refuse pond coal slurry using flotation. *Energy Sources Part A Recover. Util. Environ. Eff.* **2018**, *40*, 1250–1256. [CrossRef]
4. Yu, Y.; Ma, L.; Cao, M.; Liu, Q. Slime coatings in froth flotation: A review. *Miner. Eng.* **2017**, *114*, 26–36. [CrossRef]

5. Wang, S.; Tao, X. Comparison of flotation performances of low rank coal in air and oily bubble processes. *Powder Technol.* **2017**, *320*, 37–42. [CrossRef]
6. Xing, Y.; Gui, X.; Pan, L.; Pinchasik, B.E.; Cao, Y.; Liu, J.; Kappl, M.; Butt, H.J. Recent experi-mental advances for understanding bubble-particle attachment in flotation. *Adv. Colloid. Interfac.* **2017**, *246*, 105–132. [CrossRef] [PubMed]
7. Vinnett, L.; Contreras, F.; Yianatos, J. Gas dispersion pattern in mechanical flotation cells. *Miner. Eng.* **2012**, *26*, 80–85. [CrossRef]
8. Wang, G.; Ge, L.; Mitra, S.; Evans, G.M.; Joshi, J.; Chen, S. A review of CFD modelling studies on the flotation process. *Miner. Eng.* **2018**, *127*, 153–177. [CrossRef]
9. Schubert, H. On the optimization of hydrodynamics in fine particle flotation. *Miner. Eng.* **2008**, *21*, 930–936. [CrossRef]
10. Zhang, W. Evaluation of effect of viscosity changes on bubble size in a mechanical flotation cell. *Trans. Nonferrous Met. Soc. China* **2014**, *24*, 2964–2968. [CrossRef]
11. Karagüzel, C.; Çobanoğlu, G. Stage-wise flotation for the removal of colored minerals from feld-spathic slimes using laboratory scale Jameson cell. *Sep. Purif. Technol.* **2010**, *74*, 100–107. [CrossRef]
12. Han, Y.; Zhu, J.; Shen, L.; Zhou, W.; Ling, Y.; Yang, X.; Wang, S.; Dong, Q. Bubble Size Distribution Characteristics of a Jet-Stirring Coupling Flotation Device. *Minerals* **2019**, *9*, 369. [CrossRef]
13. Li, H.; Li, R.; Wang, M.; Li, J.; Fu, Y.; Zhu, B. Method for the adsorption of surfactants by lignite in a dry condition using mechanical mixing. *Miner. Eng.* **2020**, *157*, 106538. [CrossRef]
14. Yianatos, J.; Vallejos, P.; Matamoros, C.; Díaz, F. Froth liquid transport in a two-dimensional flotation cell. *Miner. Eng.* **2018**, *122*, 227–232. [CrossRef]
15. Laskowski, J.; Tlhone, T.; Williams, P.; Ding, K. Fundamental properties of the polyoxypropylene alkyl ether flotation frothers. *Int. J. Miner. Process.* **2003**, *72*, 289–299. [CrossRef]
16. Kracht, W.; Rebolledo, H. Study of the local critical coalescence concentration (l-CCC) of alcohols and salts at bubble formation in two-phase systems. *Miner. Eng.* **2013**, *50–51*, 77–82. [CrossRef]
17. Tomiyama, A.; Celata, G.P.; Hosokawa, S.; Yoshida, S. Terminal velocity of single bubbles in surface tension force dominant regime. *Int. J. Multiphas. Flow.* **2002**, *28*, 1497–1519. [CrossRef]
18. Krzan, M.; Zawala, J.; Malysa, K. Development of steady state adsorption distribution over interface of a bubble rising in solutions of n-alkanols (C5, C8) and n-alkyltrimethylammonium bromides (C8, C12, C16). *Colloids Surfaces A Physicochem. Eng. Asp.* **2007**, *298*, 42–51. [CrossRef]
19. Zhu, H.; Valdivieso, A.L.; Zhu, J.; Min, F.; Song, S.; Huang, D.; Shao, S. Effect of dodecylamine-frother blend on bubble rising characteristics. *Powder.Technol.* **2018**, *338*, 586–590. [CrossRef]
20. Yang, Y.; Karvounis, N.; Walther, J.H.; Ding, H.; Wen, C. Effect of area ratio of the primary nozzle on steam ejector performance considering nonequilibrium condensations. *Energy* **2021**, *237*, 121483. [CrossRef]
21. Dafsari, R.A.; Yu, S.; Choi, Y.; Lee, J. Effect of geometrical parameters of air-induction nozzles on droplet characteristics and behaviour. *Biosyst. Eng.* **2021**, *209*, 14–29. [CrossRef]
22. Bodys, J.; Smolka, J.; Palacz, M.; Haida, M.; Banasiak, K.; Nowak, A.J. Experimental and numerical study on the R744 ejector with a suction nozzle bypass. *Appl. Therm. Eng.* **2021**, *194*, 117015. [CrossRef]
23. Bodys, J.; Smolka, J.; Banasiak, K.; Palacz, M.; Haida, M.; Nowak, A.J. Performance improvement of the R744 two-phase ejector with an implemented suction nozzle bypass. *Int. J. Refrig.* **2018**, *90*, 216–228. [CrossRef]
24. Hu, L.; Xu, H.; Li, M.; Liu, W.; Chen, W.; Xie, H.; Fu, X. Liquid jet formation during a suspended liquid suction process. *Exp. Therm. Fluid Sci.* **2020**, *114*, 109952. [CrossRef]
25. Vanierschot, M.; Persoons, T.; Van den Bulck, E. A new method for annular jet control based on cross-flow injection. *Phys. Fluids* **2009**, *21*, 025103. [CrossRef]
26. Trávníček, Z.; Tesař, V.; Broučková, Z.; Peszynski, K. Annular Impinging Jet Controlled by Radial Synthetic Jets. *Heat Transf. Eng.* **2014**, *35*, 1450–1461. [CrossRef]
27. Gordiychuk, A.; Svanera, M.; Benini, S.; Poesio, P. Size distribution and Sauter mean diameter of micro bubbles for a Venturi type bubble generator. *Exp. Therm. Fluid Sci.* **2016**, *70*, 51–60. [CrossRef]
28. Sriveerakul, T.; Aphornratana, S.; Chunnanond, K. Performance prediction of steam ejector using computational fluid dynamics: Part Validation of the CFD results. *Int. J. Therm. Sci.* **2007**, *46*, 812–822. [CrossRef]
29. Zheng, H.; Su, Y.; Zheng, L.; Ke, H. Numerical simulation of CO_2 and dye separation for supercritical fluid in separator. *Sep. Purif. Technol.* **2020**, *236*, 116246. [CrossRef]
30. Akhlaghi, M.; Mohammadi, V.; Nouri, N.M.; Taherkhani, M.; Karimi, M. Multi-Fluid VoF model assessment to simulate the horizontal air–water intermittent flow. *Chem. Eng. Res. Des.* **2019**, *152*, 48–59. [CrossRef]
31. Chen, J.; Orozovic, O.; Williams, K.; Meng, J.; Li, C. A coupled DEM-SPH model for moisture migration in unsaturated granular material under oscillation. *Int. J. Mech. Sci.* **2020**, *169*, 105313. [CrossRef]
32. Chen, J.; Wang, P.; Li, M.; Shen, J.; Howes, T.; Wang, G. Rupture distance and shape of the liquid bridge with rough surface. *Miner. Eng.* **2021**, *167*, 106888. [CrossRef]
33. Sarhan, A.; Naser, J.; Brooks, G. CFD model simulation of bubble surface area flux in flotation column reactor in presence of minerals. *Int. J. Min. Sci. Technol.* **2018**, *28*, 999–1007. [CrossRef]